3D Modeling Beneath Ground: Plant Root Detection and Reconstruction Based on Ground-Penetrating Radar

Yawen Lu, Guoyu Lu
Intelligent Vision and Sensing Lab, Rochester Institute of Technology, USA

Abstract

3D object reconstruction based on deep neural networks has been gaining attention in recent years. However, recovering 3D shapes of hidden and buried objects remains to be a challenge. Ground Penetrating Radar (GPR) is among the most powerful and widely used instruments for detecting and locating underground objects such as plant roots and pipes, with affordable prices and continually evolving technology. This paper first proposes a deep convolution neural network-based anchor-free GPR curve signal detection network utilizing B-scans from a GPR sensor. The detection results can help obtain precisely fitted parabola curves. Furthermore, a graph neural network-based root shape reconstruction network is designated in order to progressively recover major taproot and then fine root branches' geometry. Our results on the gprMax simulated root data as well as the real-world GPR data collected from apple orchards demonstrate the potential of using the proposed framework as a new approach for fine-grained underground object shape reconstruction in a non-destructive way.

1. Introduction

Ground-penetrating radar (GPR) is a continually evolving, reliable and effective technology for near-surface sensing. It is generally used as a non-destructive, three-dimensional imaging method and has been widely applied to geological exploration [40], damage inspection [3] [14] [5], concrete scanning [9] [28], underground structure detection and localization [20] [21] [32] e.g., utility pipes, soil, and rebars. Due to these extraordinary properties, GPR sensors have become a powerful tool in remote sensing applications to facilitate civil engineers and geophysicists.

Nonetheless, visual interpretation of GPR data is extremely timely and labor-consuming. Usually, the GPR data collected within a day needs several weeks or even longer to be successfully interpreted by an experienced engineer. This shortcoming severely limits the efficiency of maintenance and rehabilitation. Moreover, current GPR applications mainly focus on large and thick underground objects such as pipes and rebars, making it extremely difficult to detect and locate thin plant root structures accurately. Furthermore, object reconstruction models from sampled sliced B-scans are relatively sparse, resulting in a serious loss of most fine branches. Hence, taking complicated plant root as a proxy object, we aim to address these challenges by introducing our novel pipeline that automatically detects underground root structures and recovers dense and detailed root shapes, which is illustrated in Fig. 1. Unlike existing works, our designated framework develops a deep neural network (DNN)-based method to jointly detect underground roots from GPR scans and reconstruct the trunk and branches of plant roots, which has been seldom explored in the past.

In this paper, we explore reconstructing dense root structures from multiple detected 2D GPR sensing slices. To learn the root shape precisely and accurately, we first apply a series of preprocessing steps including the time zero correction, background noise exclusion, and amplitude gain to compensate for the signal attenuation. Furthermore, we introduce an anchor-free root detection network to locate the root branches in each profile. Specifically, we propose **ParNet** to use a parabola curve to effectively represent the root feature in the processed GPR scans instead of normal rectangular bounding boxes. The detected root signal parabola is modeled with the center point of the parabola curve and the coefficients of the hyperbola equations in order to fit the root shape. In the single-forward one-stage training pass, a stacked hourglass backbone is utilized to extract image features from the processed GPR scan images, as well as output parabola center keypoint heatmaps that are used to localize the center point of the hyperbola curve. Meanwhile, the parabola coefficients are estimated to form the parabola curve together with the estimated parabola center.

Based on the sparse points generated from the detected parabolas, we further propose a graph neural network based point cloud reconstruction network (**GRecNet**) to recover the complete 3D roots. The input to **GRecNet** is a group of $N \times 3$ unordered sparse points obtained from the GPR detection. Four graph convolutional layers are applied as an encoder to map the input to a latent vector. The vector is mapped to a low-dimensional feature space and is then used to progressively generate the major root shape (e.g., taproot)

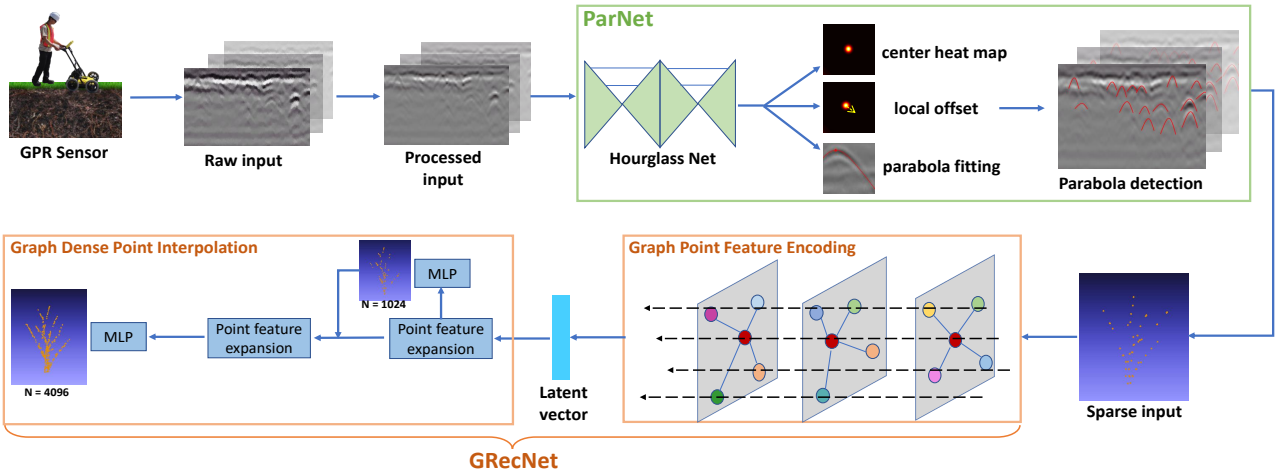

Figure 1. Overview architecture of the proposed framework. It consists of two main modules: (a) **ParNet** to automatically detect root parabola curves from the input GPR scans (Top), and (b) **GRecNet** to progressively reconstruct dense 3D root structures via a graph-based encoding and interpolation (Bottom).

and fine local geometric details for thin root branches. Different from MLP based point generation networks such as PointNet [30], our GCN based network can capture extra geometry relationships among the adjacent points, which is extremely helpful for recovering the fine-grained structures.

Our proposed framework is able to recover underground objects, thereby helping agriculturists and civil engineers to assess plant roots automatically and supporting them to further extract key traits from the roots (e.g., root branch number, root length or diameter). The most significant contributions of our designated pipeline are as follows: 1) We propose an anchor-free approach specially for fitting parabola curves in root structure detection. To the best of our knowledge, the proposed **ParNet** is the first anchor-free method to represent, detect and fit parabola curves for target shapes. 2) We propose a graph neural network to recover the fine-grained root structures by inputting the sparse detected root points. The design of the two-stage 3D reconstruction strategy progressively exploits both coarse root structure and fine details for a complete and dense point cloud. 3) Lacking of public large-scale plant root GPR data, we collect a real GPR dataset at an apple orchard, in addition to the generation of a large-scale simulated GPR scans from high-quality 3D root models for effective training. 4) Extensive experiments validate the effectiveness of the proposed framework, which outperforms state-of-the-art methods on both target detection and 3D reconstruction.

2. Related work

2.1. Conventional GPR Interpretation Methods

Conventional methods have been introduced to convert raw GPR B-scans into images with clearly observable focused targets [33] [16] [8]. [33] could localize the buried targets. However, it suffers from an unsatisfactory accuracy performance, as well as a long computation time. As an alternative to [33], a phase shift-based method [16] was presented in the frequency domain instead of configuration space. The advantage of this method is that it is computationally more efficient than [33]. Conversely, [8] is different from other mathematical-based interpolation methods as it could tackle the concealed object detection task by implementing a back-projection algorithm.

Particularly on agriculture science as experiments conducted in this paper, GPR has been explored on root diameter detection [7] [48] [27], biomass estimation [7] [49] [25] [2], root morphology mapping [17] [39] and three-dimensional reconstruction [44] [15]. Molon et al. [25] derived root structure and coarse biomass by using isolated surfaces from 1GHz GPR scans with the marching cubes algorithm. For demonstrating GPR's viability in mapping the street trees' roots path, Wu et al. [44] developed an automated root system architecture to improve the effectiveness of 3D root system reconstruction. Experiments were conducted by Conyers et al. [6] on the root location detection, biomass estimation, and root diameter of thick roots with GPR images. From the evaluations and conclusions of the above-mentioned studies, GPR images can be affected by several factors, such as root diameter, root direction, and root location. Hence, conducting extensive research to investigate new algorithms for GPR images is imperative.

2.2. Learning-based Automatic GPR Interpretation

Recently, there has been an upsurge in the use of learning-based methods [1] [11] [26], in addition to conventional interpretation methods, due to their outstanding performance in object detection. [1] implemented Hough Transform on the GPR reflection edges for the detection of buried targets and Mohamed et al. [11] were able to classify underground utility materials by extracting discrete features of cosine transform coefficients and feeding them

into a support vector machine. On the other hand, [26] further applied convolution support vector machine (CSVM) on the GPR B-scan images for reducing the computational cost and improving its performance based on [11].

The algorithm performance and reliability can be further improved through more representative and enhanced features extracted from deep neural networks. Taking Faster R-CNN as an example, efficient features can be extracted from input 2D GPR scans to obtain underground object detection [4] [29] [45] [13] [12]. Xu et al. [45] explored Faster R-CNN for detecting railway subgrade defect in order to ensure train operation safety. Feng et al. [13] extended it to first use an improved Faster-RCNN-based network for detecting buried objects, and then applied a depth estimation network to output the detected objects' depth values. Li et al. [22] presented a subsurface defect detection algorithm to generate 3D proposals and GPR-RCNN bounding boxes by fusing 2D planar features and 3D voxel-wise features. The generated proposals and bounding boxes are further utilized for 3D target detection from GPR B-scans sequences.

2.3. Point Cloud Shape Reconstruction

Most of previous learning-based shape reconstruction methods [19] [35] [36] represent 3D shapes with voxels, which is inefficient in the computation time. The point cloud is one of the most efficient representations in 3D space, and is widely used in 3D vision and remote sensing. However, it is commonly complicated to apply traditional convolutions directly on the point cloud, given its inherent unordering and random point clouds distribution. Thus, PointNet [30] is proposed to use a symmetric function for aggregation of local/global point features. In [31] [34], researchers utilize a similar technique as [30] but with considerable improvement in local feature learning. To achieve a high-quality point cloud reconstruction, a folding-based decoder was designed by Yang et al. [46] to deform a canonical 2D grid into the underlying 3D point cloud. In contrast, Yuan et al. [47] designed a learning-based dense point cloud generation network using 3D point clouds input directly, while [37] used a decoder for the hierarchical generation of point clouds following the tree structure. Though helpful in improving the performance and robustness of the reconstructed shape, these methods mainly focus on relatively large objects with uniform shape distribution, e.g., cars, bottles and chairs. Precise point cloud reconstruction for subtle and complex plant roots is rarely explored before.

3. Dense Root Reconstruction

3.1. GPR Image Sensing

A GPR sensor detects underground objects by transmitting a polarized pulse through the equipped antenna. The radar energy will be reflected back to GPR when reaching objects with different electromagnetic properties. The

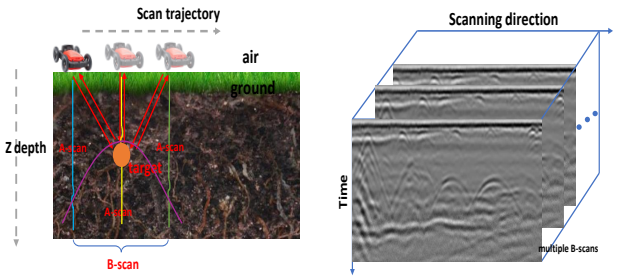

Figure 2. An illustration of the principles of GPR sensing. GPR functions through transmitting EM pulses of radio waves down into the ground via an antenna. When reaching an object with different electromagnetic properties, the pulses will be reflected back to GPR sensor (a). Multiple B-scans along the moving direction can represent the sparse 3D underground object shape (b).

GPR sensor records the traveling time from the emission to the echos, and generate one dimensional data containing the signal strength and traveling time, called A-scan. When the GPR moves along a scanning trajectory, a series of A-scans at different positions will be produced, building a 2D map called B-scan. The illustration of A-scan and B-scan is depicted on the left side of Fig. 2. If the GPR sensor is operated to move along the survey grid line (both horizontal and vertical lines), multiple parallel B-scans will be collected to construct a sparse 3D cube to record the 3D information, which is shown on the right side of Fig. 2.

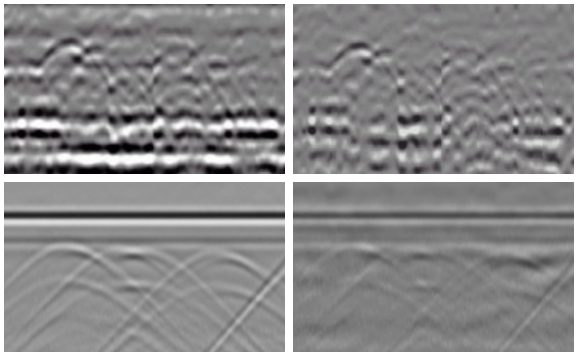

Figure 3. Pre-processing of the real and simulated GPR B-scans. Top: The real GPR image before and after pre-processing; Bottom: The simulated GPR image before and after adding noises.

Affected by the inhomogeneity of the real root structure and the impact of noises from stones and other impurities in the soil, the real GPR B-scan will contain noises that affect the final detection performance. Therefore, we apply a series of pre-processing steps to reduce the background noise and enhance the parabola features. More specifically, the raw input is first processed by a time zero correction method to adjust the scan's top signal to be close to the ground surface in order to more accurately sense the object depths. In addition, the corrected B-scan frame will be passed through a background removal filter to suppress the horizontal-like background noises caused by the antenna

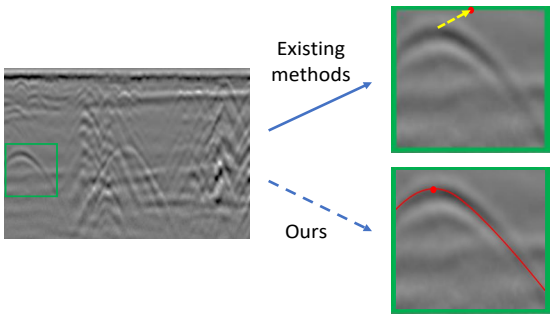

Figure 4. Motivation of the designated anchor-free **ParNet**, compared with the regular detected bounding boxes. The proposed ParNet is able to estimate and fit a more accurate and consistent parabola curve, which is particularly helpful for accurate 3D shape reconstruction step as **GRecNet**.

ringing. Lastly, a signal amplitude gain is utilized for compensating the signal attenuation, which facilitates detecting objects buried deeply underground.

Further, considering that the surrounding environment of the real-collected GPR scans is much more complex than the simulated data, we add the background noise recorded from the real GPR signals without roots onto the simulated scans. This enhances the training effect of the simulated data. Fig. 3 shows the results before and after the processing on the real data (top), and the results before and after adding the real noise on the simulated GPR scans (bottom).

3.2. Anchor-free parabola signal detection

Existing detection methods usually regress rectangular bounding boxes, as well as output dimensions of each box, which could causes relatively large errors and uncertainties in locating object depths (as illustrated in Fig. 4). Therefore, we propose an anchor-free detection network, **ParNet**, for parabola feature detection in GPR B-scans. ParNet detects object GPR signals through two sub-networks: a parabola center localization network and a parabola fitting module. Parabola center localization is developed to localize the GPR signal center. Different from the definition of the center point in CenterNet [10], for the input image $I \in R^{W \times H \times 3}$ with height H and weight W, the estimated keypoint $p^k \in R^2$ represents the center of each parabola. p^k in the parabola center localization network is defined as:

$$p^k = (x_{center}, \frac{y^k_{top} + y^k_{bot}}{2}) \tag{1}$$

where x_{center} is the abscissa of the parabola vertex, instead of the abscissa of the center point in each bounding box, and k is the number of the parabola in an image with c category. Hence, a keypoint heatmap $H \in w' \times h' \times c$ is modeled by a 2D Gaussian kernel, enabling a symmetric expression and a higher response near the parabola center, which is formulated as:

$$H_{center} = exp(-\frac{(x - \hat{p}_x)^2 + (y - \hat{p}_y)^2}{2\sigma_p^2}) \tag{2}$$

where $w' = \frac{W}{S}$, $h' = \frac{H}{S}$, and $\hat{p} = \lfloor \frac{p}{S} \rfloor$. S and σ_p^2 are the downsampling factor and parabola size adaptive kernel standard deviation.The predicted keypoint heatmap is then optimized by the center keypoint regression loss L_{center}, which is a variant of focal loss in [23] as:

$$L_{center} = -\frac{1}{N} \sum_{center} \begin{cases} (1 - \hat{H}_{center})^{\alpha} log(\hat{H}_{center}), \\ if H_{center} = 1 \\ (1 - H_{center})^{\beta} (\hat{H}_{center})^{\alpha} \\ log(1 - \hat{H}_{center}), \ else \end{cases} \tag{3}$$

where H_{center} is the ground truth modeling of the parabola center, and $\hat{H}_{center}$ is the estimated output from the parabola center localization network. α and β are two hyper-parameters in L_{center}.

To recover the discretization error caused by the different downsampling factors S, the local parabola center offset loss L_{off} is further introduced to slightly refine the inferred estimated parabola center position by considering the local offset value with an $L1$ loss as:

$$L_{off} = \frac{1}{N} \sum_{p} |\widehat{OS}_p - (\frac{p}{S} - \hat{p})| \tag{4}$$

where $\widehat{OS}_p$ is the estimated local offset for each parabola center point. In order to fit the detected parabola, we propose a parabola parameter estimation branch to output the coefficients of the parabola equations. Each target root curve is formed as an parabola with the estimated center point $\hat{p}$ with offsets δ, and the parabola coefficients a and b:

$$\begin{aligned} Par(x) &= a(x - \hat{c})^2 + b \\ \hat{c} &= (\hat{p}_x + \delta\hat{p}_x, \ \hat{p}_y + \delta\hat{p}_y) \end{aligned} \tag{5}$$

Therefore, the parabola fitting loss is optimized by $L1$ norm at each detected parabola center as:

$$L_{fitting} = \frac{1}{N} \sum_{k=1}^{N} |\hat{a} - a| + |\hat{b} - b| \tag{6}$$

Hence, the overall training objective for **ParNet** becomes:

$$L_{ParNet} = L_{center} + \lambda_1 L_{off} + \lambda_2 L_{fitting} \tag{7}$$

where λ_1 and λ_2 are parameters to balance different losses and set to be 1.0 and 0.2.

3.3. Graph-based 3D reconstruction

To comprehensively learn the fine-grained root structure, we design a novel graph neural network to capture rich geometry relationships among adjacent points. To build the graph, we encode each point as a vertex in a graph and the connection between adjacent points as edges, enabling the extracted features to flow between neighbors. Hence, a point cloud can be defined as a set $V = v_1, ...v_i, ..., v_N$. Each v_i is composed of (p_i, s_i) where $p_i \in R^3$ denotes the point in 3D space and $s_i \in R^c$ denotes the point properties with c dimension. Therefore, given each V, we are able to construct a graph structure $G = (V, E)$, by connecting vertex V to its k neighboring points through edges E.

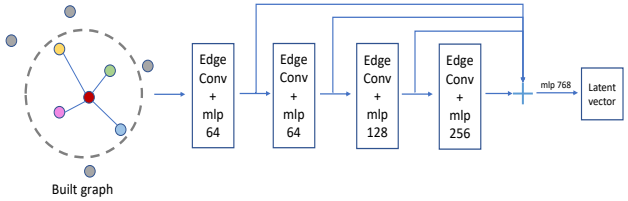

Figure 5. Point feature encoding network structure for latent vector generation.

With the graph built from the $N \times 3$ unordered sparse points, we apply a graph convolutional neural network to learn the graph features. Compared with PointNet [30] based approaches, Graph Convolutional Network (GCN) can efficiently capture geometric relationships among the points, which greatly aids the thin and fine-grained root branches. As illustrated in Fig. 5, the input graph is applied via multiple edge convolution (EdgeConv) layers [42] with 64, 64, 128 and 256 channels progressively, which is convolution-like operations on the edges connecting each neighbor pair of points. The calculated edge features after different EdgeConv layers are then aggregated together to form a global, low-dimensional and compact latent feature vector in the size of 768, after a multi-layer perceptron and a max-pooling operation.

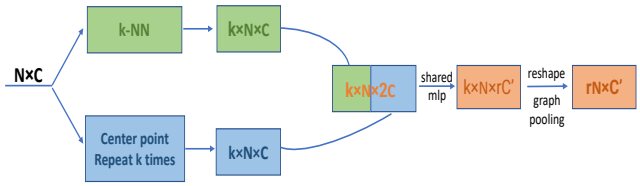

Figure 6. The architecture illustration of the point decoding module for feature expansion. With this module, the input points can be effectively interpolated progressively and smoothly.

In the generator, the latent vector is first resized to a feature space with a size of 256×3. After reshaping, the convolution network for point feature expansion progressively enlarges the point features to a high dimension, in order to recover the final dense and complete root structures. The inner structure of the point feature expansion block is detailed in Fig. 6. The input features are represented by the kNN edge feature f_{edge}^k for the k th nearest neighbor and the center point feature f_p for the center point p. Assuming $\bigoplus$ stands for the feature concatenation, S_{mlp} is the shared multi-layer perceptions, and $g(\cdot)$ represents the graph max pooling function. R stands for the reshaping operation. Given a $N \times C$ feature input, the expanded output O with a size of $rN \times C'$ can be expressed by:

$$O = g\left(R\left(S_{mlp}\left(f_p \bigoplus f_{edge}^1\right), ..., S_{mlp}(f_p \bigoplus f_{edge}^k)\right)\right) \tag{8}$$

After the point feature expansion, the point number can be upsampled by r times. Therefore, we generate an initial reconstruction with a size of 1024×3. Though the coarse root can recover the rough skeleton of the taproot, it is not sufficient to exploit detailed geometric features. We further apply the second point expansion block to generate a dense reconstruction with a dimension of 4096×3, for better refining the fine-grained details. Benefiting from the graph convolutions and point feature expansion, the reconstruction shows good performance in expanding and interpolating the current root structure with accurate and balanced point distribution, preventing simple point duplication and overlapping as exhibited in PointNet-based methods.

Two types of loss constraints are applied in **GRecNet**, from coarse to fine scales between the produced point cloud and the sampled ground truth point cloud. The symmetric Chamfer Distance (CD) is applied for calculating the distance between the coarse output and the ground truth point cloud, and the Earth Mover's Distance (EMD) is used to minimize the distance between the final fine output and the ground truth point cloud. Specifically, CD calculates the average closet point distance between two point sets. Applying CD in a symmetric way to constrain the coarse output Y_{crs} towards the ground truth Y_{gt}, L_{crs} is expressed as:

$$L_{crs} = CD(Y_{crs}, Y_{gt}) = \frac{1}{|Y_{crs}|} \sum_{x \in Y_{crs}} min_{y \in Y_{gt}} \|x - y\|_2 + \frac{1}{|Y_{gt}|} \sum_{y \in Y_{gt}} min_{x \in Y_{crs}} \|y - x\|_2 \tag{9}$$

The EMD loss is further introduced in the final fine-grained output to generate a complete point cloud:

$$L_{fine} = EMD(Y_{fine}, Y_{gt}) = \min_{\phi: Y_{fine} \to Y_{gt}} \sum_{x \in Y_{fine}} \|x - \phi(x)\|_2 \tag{10}$$

where $\phi : Y_{fine} \to Y_{gt}$ is a bijection between Y_{fine} and Y_{gt}. For each subset of point set pairs, the optimal bijection is unique and invariant under the movement of the points, enabling the EMD distance to be differentiable for each point pair. L_{fine} ensures the sum of distances between the corresponding 3D points for each group is minimal.

To further exclude the potential outliers and discontinuities in the reconstruction, a point cluster loss is introduced to penalize the point-to-neighbor distance among the adjacent 3D points:

$$L_{cluster} = \sum_{p} w_p \cdot D_{pt-to-Neighb} \tag{11}$$

$$D_{pt-to-Neighb}(p) = \frac{1}{k}(\sum_{p' \in kNN(p)} ||p - p'||_2) \tag{12}$$

where $D_{pt-to-Neighb}$ is the average Euclidean distance between each point and its k-NN neighbors. If $D_{pt-to-Neighb}$ is larger than a threshold, then w_p will be to be 1, otherwise 0. The threshold is set to be the multiple of the standard deviation of all computed distances. Based on the introduced loss functions, the compound objective function for **GRecNet** is defined as:

$$L_{GRecNet} = L_{crs} + \lambda_3 L_{fine} + \lambda_4 L_{cluster} \tag{13}$$

where λ_3 and λ_4 are parameters to balance the shape reconstruction net, and are set as 1.0 and 0.2, respectively.

4. Experiments

In this section, we subsequently describe the simulated and collected real-world GPR dataset for training the network, experimental evaluation metrics, implementation configuration, and the qualitative and quantitative results and comparisons, for both our **ParNet** and **GRecNet**. The analyses of time speed, cost and ablation studies are also provided at the end.

4.1. Dataset and Implementation Details

Dataset: In this paper, we evaluate our full pipeline on both simulated GPR scans from synthetic 3D root models, and the real collected GPR images at an apple orchard, in order to verify the proposed method's effectiveness. 200 synthetic 3D models were created using the Unity game engine's Game Object class [18]. Each one is sampled along the preset paths at a fixed frequency interval and stimulates as the GPR sensor moving. Hence, 15 cross-sections for each moving direction and 6 directions together lead to 90 cross-sections for each root. The scattered 3D points from cross-sections are further converted into 18000 2D GPR B-scans via gprMax [43]. The 2D GPR scans are labeled to serve as the ground truth detection for our **ParNet** and the compared detection approaches. The 3D Unity models are sampled in point cloud format to act as the ground truth for **GRecNet** and the compared reconstruction methods. Apart from the simulated data, a SIR-400 GPR sensor with an antenna type 800D is deployed at the apple orchard, further verifying the effectiveness of our trained **ParNet** and **GRecNet**, in a non-invasive way.

Configuration: We train our entire framework in a two-step training strategy to obtain an efficient convergence. The root parabola detection network **ParNet** is first trained for 30 epochs, and then is fine-tuned together with the graph-based root shape reconstruction network **GRecNet** for another 50 epochs with a batch size of 4. The entire pipeline is implemented on a Tesla P40 GPU with Adam optimizer as well as an initial learning rate of 1e-4 (gradually decayed to half for the last 20 epochs).

4.2. Results from ParNet Compared with Other Detection Methods

As shown in Fig. 7 and Fig. 8, we evaluate the detection performance on the simulated and real GPR scans respectively. To fairly compare different methods, all models are trained without any post-processing steps. It can be noticed that the proposed network provides accurate detection and fits precisely on parabola shapes. From Fig. 7, [13] appeared with fewer bounding boxes and missed some root targets. [24] and [27] improved with regard to the root target missing issue, but with loose boundaries and false and overlapping bounding box estimations. In contrast, our method is able to recover tight and accurate parabola curve, instead of the rough rectangular bounding boxes only. From Fig. 8, we can observe that though [24] and [13] achieve relatively correct regressions on the rectangular boxes, ours can locate the exact vertex point by fitting the parabola equations.

Method	Backbone	AP	AP-50	AP-75
CenterNet-52 [10]	Hourglass-52	0.840	0.874	0.853
Liu et al. [24]	VGG-16	0.784	0.870	0.802
Feng et al. [13]	ResNet-50	0.831	0.870	0.841
Feng et al. [13]	ResNet-101	0.834	0.872	0.839
Park et al. [27]	Darknet-53	0.771	0.863	0.797
Ours	Hourglass-52	**0.867**	**0.902**	**0.869**

Table 1. Quantitative comparisons of our root target detection with [10], [24], [13] and [27] on the simulated 2D GPR scans.

We further report the quantitative performance in Table 1, including average precision at different IoU ranging from 50% to 95% at 5% step-size (AP), average precision with IoU threshold at 0.5 ($AP50$) and at 0.75 ($AP75$). The proposed method outperforms all the comparisons with a large margin, especially in AP and $AP75$, with an improvement of 12% and 9% over [27]. The later analysis in time performance and computational cost also shows that our method can achieve high precision without additional cost.

4.3. Results from GRecNet Compared with Other Reconstruction Methods

Firstly, we evaluate **GRecNet** on the test set of the created 2D GPR dataset. The visual comparisons are demonstrated in Fig. 9. To fairly compare the reconstruction performance between different methods, we use the sparse points all detected from our **ParNet** as input. From Fig. 9,

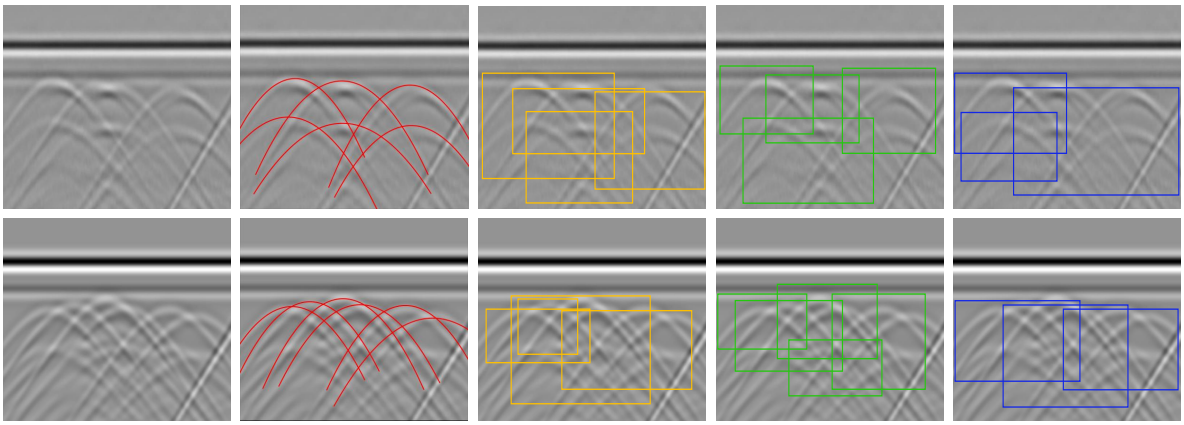

Figure 7. The qualitative results of the root parabola detection compared with other recent root detection methods on the simulated scans. Left to right: Raw created B-scans; Detection from our **ParNet**, [24], [27], and [13].

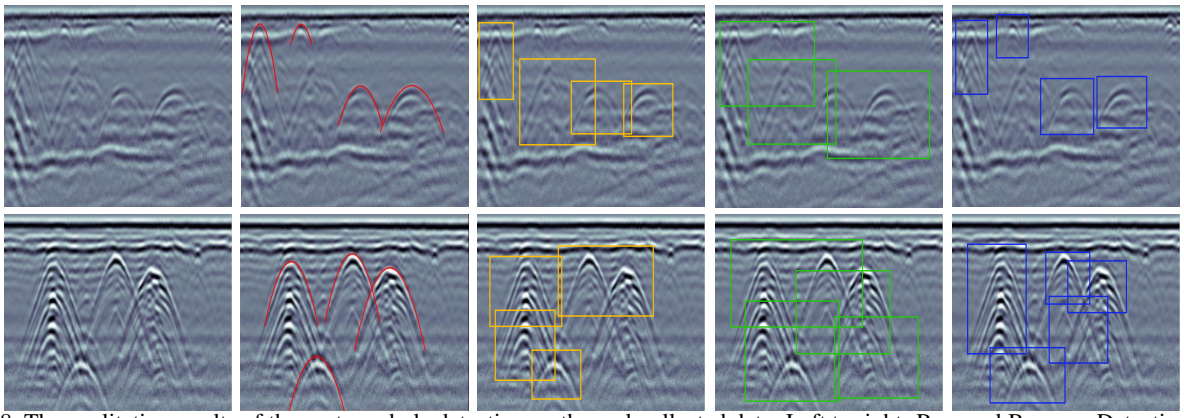

Figure 8. The qualitative results of the root parabola detection on the real-collected data. Left to right: Raw real B-scans; Detections from our **ParNet**, [24], [27], and [13].

	CD / EMD			
Object Id	PCN [47]	Wang et al. [41]	TopNet [38]	Ours
001	2.98 / 7.54	2.47 / 6.27	2.37 / 6.02	**1.91 / 4.85**
002	3.70 / 8.01	3.48 / 8.18	3.20 / 7.99	**2.07 / 5.37**
003	3.91 / 8.17	3.39 / 7.96	3.42 / 7.25	**1.76 / 5.11**
004	3.07 / 6.98	2.92 / 6.67	2.74 / 6.23	**2.30 / 4.96**
005	2.79 / 7.16	2.76 / 6.53	2.58 / 6.16	**1.93 / 4.89**
Mean	3.29 / 7.57	3.00 / 7.12	2.86 / 6.73	**1.99 / 4.94**

Table 2. Quantitative root shape reconstruction results. CD and EMD are both scaled by 100. The result is reported on five independent roots from the test set. For EMD and CD, lower is better.

we can observe the proposed method can interpolate the input sparse point uniformly and densely, and recover the thin and complicated branches without stretching and distortion. In contrast, the reconstructed structure from [47] contains extensive ambiguities and overlapping. The reconstruction from [41] suppresses the appearance of the ambiguities and noisy points. However, the root structure is still not easy to be discerned clearly, with some overlapping and stretching in the middle. [38] can recover the rough trunks, but loses a significant amount of thin branches. The reconstruction from **GRecNet** on the real data is provided in Fig. 10.

We then report the quantitative comparisons in Table 2. Both Chamfer Distance (CD) and Earth Mover's Distance (EMD) are calculated on the reconstructed point clouds and the sampled ground truth roots with 4096 3D points.

Method	PCN [47]	Wang et al. [41]	TopNet [38]	Ours
# Params	22.15 M	28.26 M	23.48 M	**18.78 M**
Speed (sec/sample)	1.24	3.82	1.72	**0.79**

Table 3. Comparisons regarding the number of model trainable parameters and the inference speed in second / sample.

4.4. Computational Cost and Ablation Studies

We compare the cost of the proposed framework with other methods in terms of the number of trainable parameters and the inference speed, as Table 3. As [47], [41] and [38] only focus on reconstruction without detection, we apply our detection network as the input to those networks. Though achieving low-error detection and reconstruction, our method does not add extra computational cost.

We analyze the effects of different losses and components on the reconstruction accuracy in Table 4. The results show that the designs of root parabola fitting, reconstruction refinement stage and the point cluster loss are useful to the final generation of the complete and dense 3D shapes. With the contributions from all of the three optimizations, the CD and EMD have a 39.8% and 32.3% decrease com-

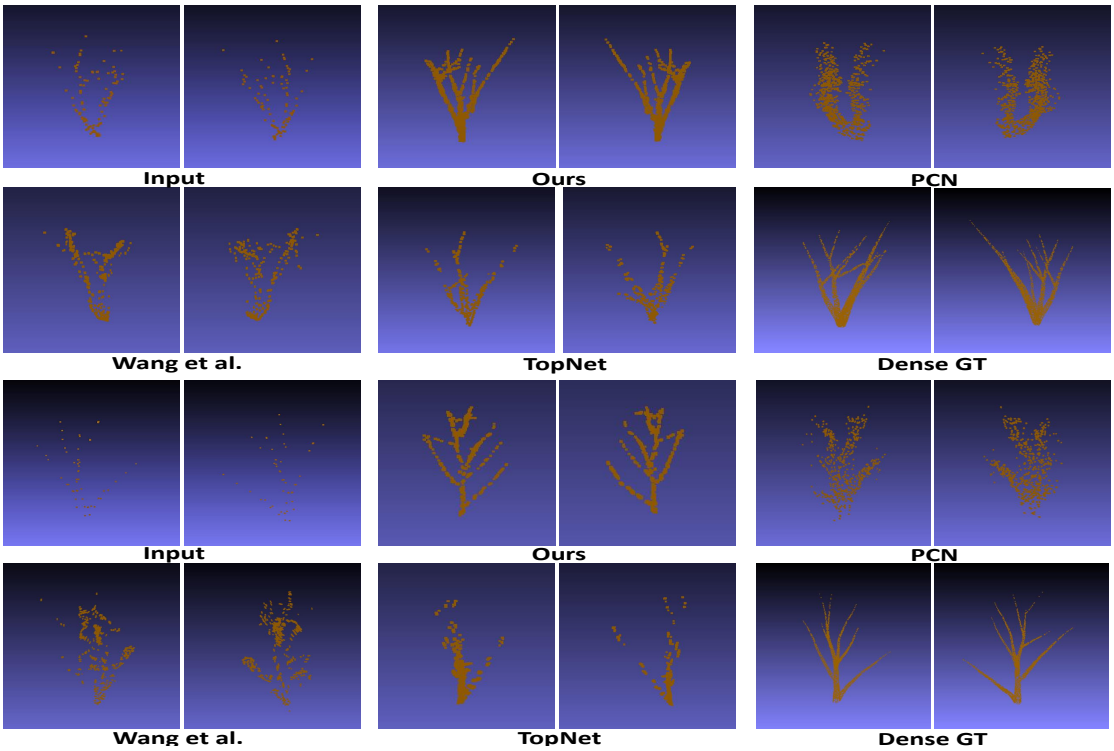

Figure 9. Qualitative comparisons of our reconstructed root structures on the simulated GPR data with PCN [47], Wang et al. [41] and TopNet [38]. Each root is demonstrated in two different views for all the methods.

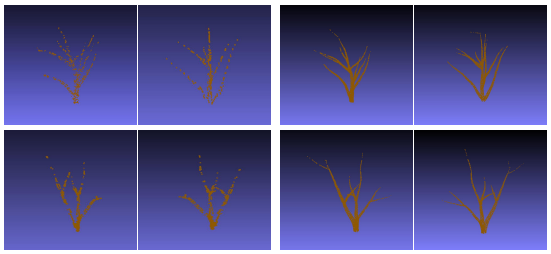

Figure 10. Qualitative reconstructions on the real GPR scans. For each root sample (row), left side are our reconstruction results at two perspectives while the right side are the ground truth root images at the same perspectives.

pared with the baseline without them. Finally, we test the different number of nearest neighbor (k) when building the graph and different output point numbers on reconstruction, as Table 5 and Table 6. We find that a large k (32) will degrade the reconstruction, and k=16 (our choice) performs the least errors. Though denser points can contribute to smaller errors, it will also result in an increase in computation cost. Hence, we choose to reconstruct 4096 points as the final output as a trade-off between accuracy and cost.

Parabola fitting	Refinement	Cluster	CD	EMD
-	-	-	3.22	7.49
✓	-	-	2.92	6.89
✓	✓	-	2.20	5.65
✓	✓	✓	**1.94**	**5.07**

Table 4. The effect of the parabola fitting, point reconstruction refinement, and the point cloud cluster loss.

# NN (k)	CD	EMD
4	2.23	5.71
8	2.19	5.62
16	**1.94**	**5.07**
32	2.02	5.18

Table 5. Results of various nearest neighbor numbers.

# Dense points	CD	EMD
2048	2.82	6.79
3072	2.36	6.11
4096	1.94	5.07
8192	**1.61**	**4.43**

Table 6. Results of different output point numbers.

5. Conclusion

In this work, we propose a novel GPR-based root parabola detection and shape reconstruction framework in a non-destructive manner. The designated root parabola detection net **ParNet** can achieve accurate parabola shape detection and curve fitting from GPR scans without anchors. And the root shape reconstruction network **GRecNet** exploits the usage of graph convolutional network to progressively recover the detailed and complex root structures. Extensive experiments demonstrate that the proposed method performs superior GPR signal detection and underground object reconstruction on both simulated and real data, and outperforms state-of-the-art methods. With the reconstructed fine-grained 3D roots, further applications can be explored, such as root trait extraction, root diameter and plant growth estimation, etc.

Acknowledgement

This work was supported by the Engineering for Agricultural Systems program through the USDA National Institute of Food and Agriculture under Grant 2021-67021-34199.

References

[1] W Al-Nuaimy, Y Huang, M Nakhkash, MTC Fang, VT Nguyen, and A Eriksen. Automatic detection of buried utilities and solid objects with gpr using neural networks and pattern recognition. *Journal of applied Geophysics*, 43(2-4):157–165, 2000.

[2] AM Alani, L Bianchini Ciampoli, Livia Lantini, Fabio Tosti, and Andrea Benedetto. Mapping the root system of matured trees using ground penetrating radar. In *2018 17th International Conference on Ground Penetrating Radar (GPR)*, pages 1–6. IEEE, 2018.

[3] Andrea Benedetto, Fabio Tosti, Luca Bianchini Ciampoli, and Fabrizio D'amico. An overview of ground-penetrating radar signal processing techniques for road inspections. *Signal processing*, 132:201–209, 2017.

[4] Lance E Besaw and Philip J Stimac. Deep convolutional neural networks for classifying gpr b-scans. In *Detection and Sensing of Mines, Explosive Objects, and Obscured Targets XX*, volume 9454, page 945413. International Society for Optics and Photonics, 2015.

[5] S Colagrande, D Ranalli, and M Tallini. Gpr research on damaged road pavements built in cut and fill sections. *Transportation Research Procedia*, 45:30–37, 2020.

[6] Lawrence B Conyers. *Ground-penetrating radar for archaeology*. AltaMira Press, 2013.

[7] XiHong Cui, Jin Chen, JinSong Shen, Xin Cao, XueHong Chen, and XiaoLin Zhu. Modeling tree root diameter and biomass by ground-penetrating radar. *Science China Earth Sciences*, 54(5):711–719, 2011.

[8] Sevket Demirci, Harun Cetinkaya, Enes Yigit, Caner Ozdemir, and Alexey A Vertiy. A study on millimeter-wave imaging of concealed objects: Application using back-projection algorithm. *Progress In Electromagnetics Research*, 128:457–477, 2012.

[9] Kien Dinh, Nenad Gucunski, and Trung H Duong. Migration-based automated rebar picking for condition assessment of concrete bridge decks with ground penetrating radar. *NDT & E International*, 98:45–54, 2018.

[10] Kaiwen Duan, Song Bai, Lingxi Xie, Honggang Qi, Qingming Huang, and Qi Tian. Centernet: Keypoint triplets for object detection. In *Proceedings of the IEEE/CVF International Conference on Computer Vision*, pages 6569–6578, 2019.

[11] Mohamed S El-Mahallawy and Mazlan Hashim. Material classification of underground utilities from gpr images using dct-based svm approach. *IEEE Geoscience and Remote Sensing Letters*, 10(6):1542–1546, 2013.

[12] Zheng Fang, Zhensheng Shi, Xiaokai Wang, and Wenchao Chen. Roadbed defect detection from ground penetrating radar b-scan data using faster rcnn. In *IOP Conference Series: Earth and Environmental Science*, volume 660, page 012020. IOP Publishing, 2021.

[13] Jinglun Feng, Liang Yang, Haiyan Wang, Yifeng Song, and Jizhong Xiao. Gpr-based subsurface object detection and reconstruction using random motion and depthnet. In *2020 IEEE International Conference on Robotics and Automation (ICRA)*, pages 7035–7041. IEEE, 2020.

[14] Francisco M Fernandes and Jorge C Pais. Laboratory observation of cracks in road pavements with gpr. *Construction and Building Materials*, 154:1130–1138, 2017.

[15] Robert S Freeland. Surveying the near-surface fibrous citrus root system of the orange tree with 3-d gpr. *Applied Engineering in Agriculture*, 32(2):145–153, 2016.

[16] Jenö Gazdag. Wave equation migration with the phase-shift method. *Geophysics*, 43(7):1342–1351, 1978.

[17] Kevin H Gormally, Marla S McIntosh, Anthony N Mucciardi, and Gregory W McCarty. Ground-penetrating radar detection and three-dimensional mapping of lateral macropores: Ii. riparian application. *Soil Science Society of America Journal*, 75(4):1236–1243, 2011.

[18] John K Haas. A history of the unity game engine. 2014.

[19] Xiaoguang Han, Zhen Li, Haibin Huang, Evangelos Kalogerakis, and Yizhou Yu. High-resolution shape completion using deep neural networks for global structure and local geometry inference. In *Proceedings of the IEEE international conference on computer vision*, pages 85–93, 2017.

[20] Man-Sung Kang, Namgyu Kim, Jong Jae Lee, and Yun-Kyu An. Deep learning-based automated underground cavity detection using three-dimensional ground penetrating radar. *Structural Health Monitoring*, 19(1):173–185, 2020.

[21] Wentai Lei, Jiabin Luo, Feifei Hou, Long Xu, Ruiqing Wang, and Xinyue Jiang. Underground cylindrical objects detection and diameter identification in gpr b-scans via the cnn-lstm framework. *Electronics*, 9(11):1804, 2020.

[22] Haifeng Li, Nansha Li, Renbiao Wu, Huaichao Wang, Zhongcheng Gui, and Dezhen Song. Gpr-rcnn: An algorithm of subsurface defect detection for airport runway based on gpr. *IEEE Robotics and Automation Letters*, 6(2):3001–3008, 2021.

[23] Tsung-Yi Lin, Priya Goyal, Ross Girshick, Kaiming He, and Piotr Dollár. Focal loss for dense object detection. In *Proceedings of the IEEE international conference on computer vision*, pages 2980–2988, 2017.

[24] Hai Liu, Chunxu Lin, Jie Cui, Lisheng Fan, Xiongyao Xie, and Billie F Spencer. Detection and localization of rebar in concrete by deep learning using ground penetrating radar. *Automation in Construction*, 118:103279, 2020.

[25] Michelle Molon, Joseph I Boyce, and M Altaf Arain. Quantitative, nondestructive estimates of coarse root biomass in a temperate pine forest using 3-d ground-penetrating radar (gpr). *Journal of Geophysical Research: Biogeosciences*, 122(1):80–102, 2017.

[26] Umut Ozkaya, Farid Melgani, Mesay Belete Bejiga, Levent Seyfi, and Massimo Donelli. Gpr b scan image analysis with deep learning methods. *Measurement*, 165:107770, 2020.

[27] Sehwan Park, Jinpyung Kim, Kyoyoung Jeon, Junkyeong Kim, and Seunghee Park. Improvement of gpr-based rebar diameter estimation using yolo-v3. *Remote Sensing*, 13(10):2011, 2021.

[28] Sepehr Pashoutani and Jinying Zhu. Ground penetrating radar data processing for concrete bridge deck evaluation. *Journal of Bridge Engineering*, 25(7):04020030, 2020.

[29] Minh-Tan Pham and Sébastien Lefèvre. Buried object detection from b-scan ground penetrating radar data using faster-rcnn. In *IGARSS 2018-2018 IEEE International Geoscience*

and Remote Sensing Symposium, pages 6804–6807. IEEE, 2018.

[30] Charles R Qi, Hao Su, Kaichun Mo, and Leonidas J Guibas. Pointnet: Deep learning on point sets for 3d classification and segmentation. In *Proceedings of the IEEE conference on computer vision and pattern recognition*, pages 652–660, 2017.

[31] Charles R Qi, Li Yi, Hao Su, and Leonidas J Guibas. Pointnet++: Deep hierarchical feature learning on point sets in a metric space. *arXiv preprint arXiv:1706.02413*, 2017.

[32] Ji-Young Rhee, Keon-Tae Park, Jin-Woo Cho, and Sang-Yum Lee. A study of the application and the limitations of gpr investigation on underground survey of the korean expressways. *Remote Sensing*, 13(9):1805, 2021.

[33] William A Schneider. Integral formulation for migration in two and three dimensions. *Geophysics*, 43(1):49–76, 1978.

[34] Yiru Shen, Chen Feng, Yaoqing Yang, and Dong Tian. Mining point cloud local structures by kernel correlation and graph pooling. In *Proceedings of the IEEE conference on computer vision and pattern recognition*, pages 4548–4557, 2018.

[35] Edward J Smith and David Meger. Improved adversarial systems for 3d object generation and reconstruction. In *Conference on Robot Learning*, pages 87–96. PMLR, 2017.

[36] David Stutz and Andreas Geiger. Learning 3d shape completion from laser scan data with weak supervision. In *Proceedings of the IEEE Conference on Computer Vision and Pattern Recognition*, pages 1955–1964, 2018.

[37] Lyne P Tchapmi, Vineet Kosaraju, Hamid Rezatofighi, Ian Reid, and Silvio Savarese. Topnet: Structural point cloud decoder. In *Proceedings of the IEEE/CVF Conference on Computer Vision and Pattern Recognition*, pages 383–392, 2019.

[38] Lyne P Tchapmi, Vineet Kosaraju, S. Hamid Rezatofighi, Ian Reid, and Silvio Savarese. Topnet: Structural point cloud decoder. In *The IEEE Conference on Computer Vision and Pattern Recognition (CVPR)*, 2019.

[39] Fabio Tosti, Luca Bianchini Ciampoli, Maria Giulia Brancadoro, and Amir Alani. Gpr applications in mapping the subsurface root system of street trees with road safety-critical implications. *Advances in transportation studies*, 44, 2018.

[40] Honghua Wang, Hai Liu, Jie Cui, Xiangyun Hu, and Motoyuki Sato. Velocity analysis of cmp gathers acquired by an array gpr system 'yakumo': results from field application to tsunami deposits. *Exploration Geophysics*, 49(5):669–674, 2018.

[41] Xiaogang Wang, Marcelo H Ang Jr, and Gim Hee Lee. Point cloud completion by learning shape priors. 2020.

[42] Yue Wang, Yongbin Sun, Ziwei Liu, Sanjay E Sarma, Michael M Bronstein, and Justin M Solomon. Dynamic graph cnn for learning on point clouds. *Acm Transactions On Graphics (tog)*, 38(5):1–12, 2019.

[43] Craig Warren, Antonios Giannopoulos, and Iraklis Giannakis. gprmax: Open source software to simulate electromagnetic wave propagation for ground penetrating radar. *Computer Physics Communications*, 209:163–170, 2016.

[44] Yuan Wu, Li Guo, Xihong Cui, Jin Chen, Xin Cao, and Henry Lin. Ground-penetrating radar-based automatic reconstruction of three-dimensional coarse root system architecture. *Plant and soil*, 383(1):155–172, 2014.

[45] Xinjun Xu, Yang Lei, and Feng Yang. Railway subgrade defect automatic recognition method based on improved faster r-cnn. *Scientific Programming*, 2018, 2018.

[46] Yaoqing Yang, Chen Feng, Yiru Shen, and Dong Tian. Foldingnet: Point cloud auto-encoder via deep grid deformation. In *Proceedings of the IEEE Conference on Computer Vision and Pattern Recognition*, pages 206–215, 2018.

[47] Wentao Yuan, Tejas Khot, David Held, Christoph Mertz, and Martial Hebert. Pcn: Point completion network. In *2018 International Conference on 3D Vision (3DV)*, pages 728–737. IEEE, 2018.

[48] Katerina Zajícová and Tomas Chuman. Application of ground penetrating radar methods in soil studies: A review. *Geoderma*, 343:116–129, 2019.

[49] Shiping Zhu, Chunlin Huang, Yi Su, and Motoyuki Sato. 3d ground penetrating radar to detect tree roots and estimate root biomass in the field. *Remote Sensing*, 6(6):5754–5773, 2014.